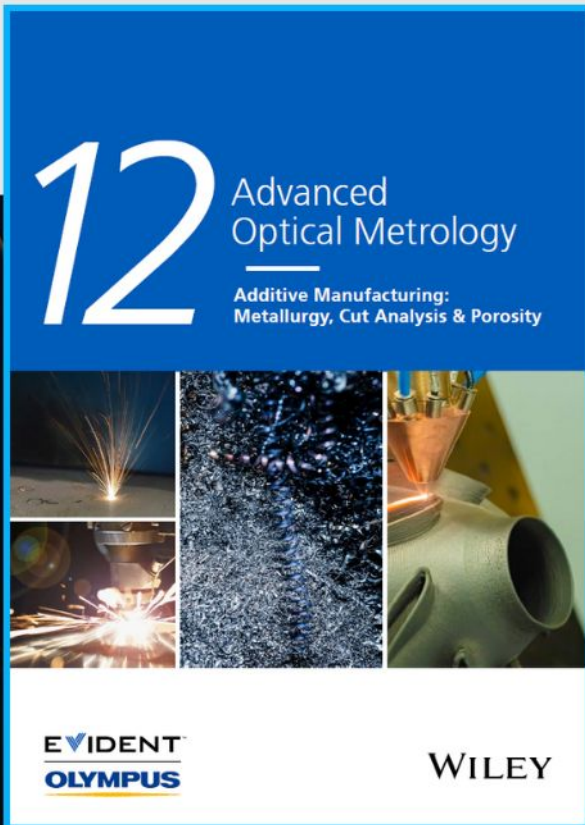




Additive Manufacturing: Metallurgy, Cut Analysis & Porosity



The latest eBook from
Advanced Optical Metrology.
Download for free.

In industry, sector after sector is moving away from conventional production methods to additive manufacturing, a technology that has been recommended for substantial research investment.

Download the latest eBook to read about the applications, trends, opportunities, and challenges around this process, and how it has been adapted to different industrial sectors.

EVIDENT™
OLYMPUS

WILEY

A New Strategy of Coupling Pyroelectric and Piezoelectric Effects for Photoresponse Enhancement of a Cu(In,Ga)Se₂ Heterojunction Photodetector

Jihong Liu, Zidong Liang, Jingwei Chen,* Shufang Wang, Caofeng Pan,* and Shuang Qiao*

Pyro/piezoelectric effects are thought as essential ways to modulate photoresponses of optoelectronic devices, but the pyro/piezoelectric materials usually function as photoactive or fundamental band matching layers. In this manuscript, a Cu(In,Ga)Se₂ (CIGS) multilayer heterojunction of Glass/Mo/CIGS/CdS/ZnO nanowire/ITO is prepared as a self-powered photodetector (PD). The PD exhibits excellent performances in 405 to 1064 nm with maximum responsivity (R) of 0.455 A W⁻¹, and detectivity (D) of 7.22×10^{11} Jones at zero bias. More importantly, the temperature variation-induced pyroelectric field in the non-photoactive ZnO layer is demonstrated to facilitate the transport of carriers. After introducing the pyroelectric effect, the responsivity (R) and detectivity (D) are largely increased to 4.92 A W⁻¹ and 7.81×10^{12} Jones, respectively, and an ultrafast response time of 67.13/78.57 μ s is obtained. Meanwhile, the response wavelength is extended to 1550 nm, which is far beyond the spectral limitation of the heterojunction. Besides, the piezoelectric effect of the ZnO nanowire can further optimize the band alignment and then boost the photovoltaic and pyroelectric responses. Owing to the favorable three-synergistic mechanisms, the best R of 7.22 A W⁻¹ and D of 1.17×10^{13} Jones are observed, which are enhanced by 1586.8% and 1620.5%, respectively, and the response time is also shortened to 50.17/60.65 μ s.

intelligent optoelectronic systems. Till now, PDs have been widely applied in various different fields, e.g. optical imaging,^[1] communication,^[2] environmental monitoring,^[3] biological sensing,^[4] and motion detection,^[5] and are also thought to promising units in some emerging areas;^[6] thus they have been widely concerned and increasingly investigated, especially with outstanding performances of high sensitivity, fast speed, and broadband spectral range. Not only that, with the growing requirements of low-cost and high energy-efficiency in the optoelectronic industry, self-powered capability,^[7] which can make PDs work well independently of external power supply in an extremely stable and sustainable manner, has become highly demanded. Based on this concept, researchers have always been trying their best to study and develop newly high-performance self-powered PDs.^[8] Generally, there are mainly two kinds of self-powered PD. One is to design the device using the photovoltaic effect,^[9,10] which operates with a built-in field in

the homo/heterojunction interface; the other is to integrate an optical sensor with an energy harvesting or storage unit.^[11,12] By comparison, the first kind is relatively easier to realize due to its simple structure, facile manufacture, and low price as the photovoltaic effect naturally exists in most semiconductor heterojunctions. Besides, the working principle of the photovoltaic effect is the same as that of the solar cells, which usually have highly efficient energy conversions and mature preparation processes, thus, it is favorable to achieve industrial production and commercial applications. Therefore, to better promote these advantages, significant efforts have been made to optimize the solar cell configurations and even design advanced materials or special structures toward efficient interfacial transfer of photo-generated carriers, and till now some PDs have been successfully prepared with exceptional self-powered properties.^[13–16] However, most of PDs are still confronted with low photoresponses due to the disadvantage of only one kind of energy conversion mechanism, which has been a severe obstacle to satisfying the growing requirements of advanced optoelectronic devices in terms of high sensitivity, energy-efficiency, and cost-saving. Besides, the

1. Introduction

Photodetectors (PDs), which transform light signals into electric signals, are one of the significant building blocks in

J. Liu, Z. Liang, J. Chen, S. Wang, S. Qiao
Hebei Key Laboratory of Optic-Electronic Information and Materials
College of Physics Science and Technology
Hebei University
Baoding 071002, P. R. China
E-mail: chenjingwei@hbu.edu.cn; sqiao@hbu.edu.cn

C. Pan
CAS Center for Excellence in Nanoscience
Beijing Key Laboratory of Micro-nano Energy and Sensor
Beijing Institute of Nanoenergy and Nanosystems
Chinese Academy of Sciences
Beijing 101400, P. R. China
E-mail: cpan@binn.cas.cn

 The ORCID identification number(s) for the author(s) of this article can be found under <https://doi.org/10.1002/adfm.202208658>.

DOI: 10.1002/adfm.202208658

spectral response range is mainly confined to the visible or near-infrared region considering the optimal absorption and conversion of the solar energy in this range,^[17,18] limiting their applications in various fields. Therefore, to vastly enhance the performances and broaden the spectrum area, newly multifunctional self-powered PDs, which could harvest or utilize multiple energy sources simultaneously with the help of multi-mechanism coupling methods, are urgently needed to explore.

Recently, the pyroelectric effect is thought as an efficient method to tune the energy band diagrams, facilitate the separation or transport of carriers across the interfaces, and thus result in the improved performances of the optoelectronic devices.^[19] In particular, it can be well coupled with the photovoltaic effect only when exposed to a pulse illumination with no any other complex preparation technologies and processes.^[20] Besides, the pyroelectric effect could also extend the response spectra to a longer wavelength,^[21] which would overcome the serious disadvantage of a narrow response range in most semiconductors. For these reasons, various novel PDs have been designed by considering the synergy of the photovoltaic effect and pyroelectric effect in some asymmetry semiconductor-based heterojunctions, such as ZnO and CdS.^[19,21–30] However, in the previous results, the pyroelectric semiconductors are either used as photoactive layers or as effective energy band functional materials matching with the photoactive layers in the heterojunctions, meaning that the temperature variation-induced pyroelectric polarization field in them can directly manipulate the separation and transport of the photo-excited carriers in the interfaces, so that the modulations are relatively easy to achieve, and the effects are expected to be considerable. In contrast, owing to the wide bandgaps of the ZnO and CdS, both of them are not suitable to play the part of the photoactive layers in the solar cells. Even though the CdS can be prepared as an energy band buffer material in contact with the photoactive layers in some heterojunctions, it is amorphous with a very thin thickness.^[15,31] Therefore, it seems that the introduction of the pyroelectric effect is not feasible in solar cell structures. Fortunately, although the ZnO cannot function as a photoactive layer, it is a vital energy level transition window material or transparent conductive material in the solar cells,^[32] the pyroelectric effect that may also be used to modify the optoelectronic processes. It is worth noting that, quite different from the previous results, the coupling modulation does not happen directly in the interface of the photo-generated carriers. Therefore, the modulation effect and mechanism are still unknown, and the related experimental and theoretical issues are urgently needed to be studied and solved. Besides, similar to the pyroelectric effect, the piezoelectric effect has also resulted from the polarization charges induced in the ZnO, thus it is promising that the photovoltaic, pyroelectric and piezoelectric effects can be mutually coupled for further enhancement of the performances in the solar cell structure-based PDs.^[33–35]

In this manuscript, a Cu(In,Ga)Se₂ (CIGS) multilayer solar cell heterojunction of Glass/Mo/CIGS/CdS/ZnO nanowire/ITO is successfully prepared by replacing the traditional ZnO film with the ZnO nanowire arrays to form a self-powered PD. The PD can achieve a broadband response range of 405 to 1064 nm, and exhibits outstanding performances at zero bias with maximum responsivity (R) of 0.455 A W⁻¹, and detectivity (D) of 7.22 × 10¹¹ Jones.

It is demonstrated that the temperature variation-induced pyroelectric potential in the ZnO nanowire can efficiently accelerate the transport of the separated carriers in the interface of the ZnO/CdS. When the pyroelectric effect is introduced, the photoresponse performances are largely improved with the R reaching up to 4.92 A W⁻¹ for an increment of 1081.3%, the D as high as 7.81 × 10¹² Jones for an increment of 1081.7%, and also an ultrafast response time of 67.13/78.57 μs, all of that are unprecedentedly better than the previous results in the similar structures. More importantly, the response wavelength is enlarged to a longer wavelength of 1550 nm, which is far beyond the spectral limitation of the CIGS heterojunction. In addition, the piezoelectric effect within the ZnO nanowire can also be utilized to optimize the band alignment of the ZnO/CdS junction and then further facilitate the improvement of the photovoltaic and pyroelectric responses. Under a pulse illumination of 500 Hz and external vertical pressure of 2 MPa, the best R of 7.22 A W⁻¹ and D of 1.17 × 10¹³ Jones are obtained, which is enhanced by 1586.8% and 1620.5%, respectively, and the response time is also shortened to 50.17/60.65 μs, indicating the favorable three-synergistic mechanisms of the photovoltaic, pyroelectric and piezoelectric effects in the CIGS heterostructure. This work indicates that the indirect modulations by the pyroelectric and piezoelectric effects in the window layer of the ZnO nanowire arrays can also be an effective strategy to tune the photovoltaic responses of the CIGS solar cell structure, and brings inspiration to modulating the performances of other multilayer heterostructures via the introduction of the pyro/piezoelectric materials and the associated effects.

2. Experimental Section

2.1. Fabrication Processes of the CIGS Heterojunction Self-Powered PD

The commercially purchased soda-lime glass (with ≈72% SiO₂, ≈15% Na₂O, and ≈9% CaO) polished on both sides was used as the substrate with a thickness of ≈2 mm. At first, the substrate was cleaned with acetone, ethanol and deionized water, sequentially, and dried with nitrogen; then the substrate was loaded into the magnetron sputtering chamber for preparation of the bottom electrode, and a ≈500 nm-thick Mo film was deposited; third, a co-evaporation system equipped with four different sources of Cu, In, Ga, and Se was used to prepare the CIGS layer, the thickness of that was ≈2 μm; fourth, the substrate was immersed into a chemical bath deposition container, in where a 80 nm-thick amorphous CdS layer was grown at 80 °C and then annealed at 135 °C for 10 min; subsequently, a ≈50 nm-thick ZnO film was prepared on the CdS as the seed layer, and then the ZnO nanowire arrays were synthesized in a mixed nutrient solution of zinc nitrate hexahydrate and hexamethylenetetramine with a concentration of 0.06 mol L⁻¹; finally, an ITO transparent conductive layer was prepared on the ZnO by the magnetron sputtering.

2.2. Material Characterizations

The crystal structure of the Glass/Mo/CIGS/CdS/ZnO nanowire/ITO heterojunction was characterized by X-ray diffraction

(XRD) (Bruker, D8 Advance), and the cross-sectional and top-view morphology was determined by a scanning electron microscope (SEM) (FEI Nova NanoSe M450).

2.3. Photoelectrical Measurements

The current-voltage (I - V) curves of the PD were measured with a Keithley 4200-SCS semiconductor system, and a continuous wave laser was used as the illumination source with wavelengths of 405, 532, 671, 808, 1064, and 1550 nm. The I - t curves of the PD were identified by a home-built system with a Stanford SRS function generator (DS345) and a low noise current preamplifier (SR570) combined by a GPIB controller (GPIB-USB-HS, NI 488.2). The pulse illumination was obtained by a mechanical chopper, and the frequency could be continuously changed from 1 to 500 Hz.

3. Results and Discussion

The structure diagram of the CIGS multilayer heterojunction PD is shown in Figure 1a. Obviously, different from the traditional CIGS solar cell structure,^[15,31,32] here, the ZnO film was replaced with ZnO nanowire arrays. There are mainly two reasons for this: one is that the ZnO nanowire arrays are thought to be favorable to the longitudinal transport of the carriers due to their excellent crystalline and considerable carrier mobility along the nanowire direction;^[36] the other is that it is easy to achieve the pyro/piezoelectric effect and then utilized to tune the performances.^[37,38] Besides, a hollow circular Ag layer was deposited as the top electrode with an illumination hole diameter of 1 mm, and a polydimethylsiloxane (PDMS) layer was prepared on the device to make sure the pressure was softly applied on it. The cross-sectional image of the scanning electron microscopy (SEM) illustrated in Figure 1b indicates a

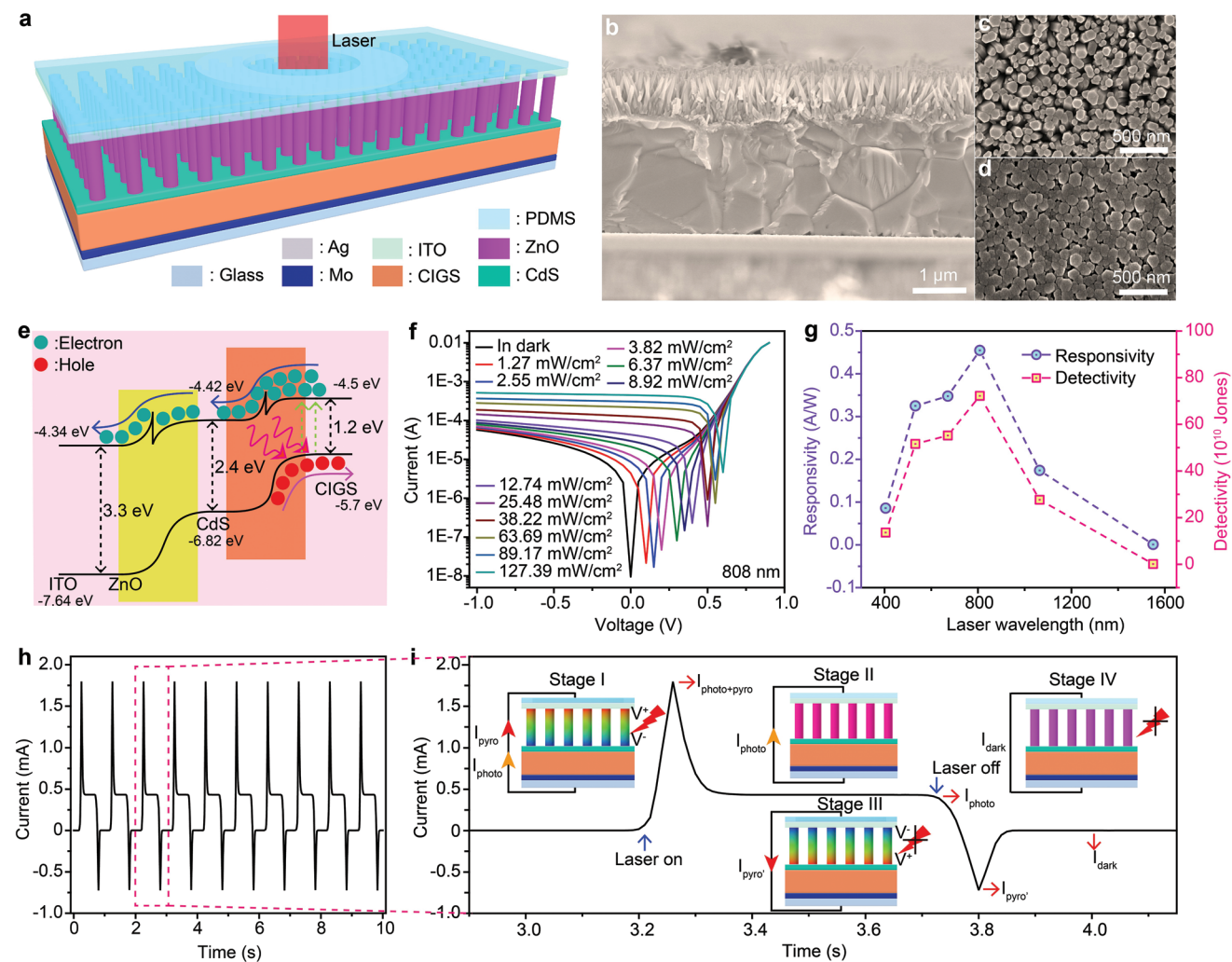


Figure 1. a) Structural diagram of the CIGS multilayer heterojunction PD. b) Cross-sectional view SEM microscopy of the CIGS heterojunction. Top view SEM microscopy of the ZnO nanowire arrays c) before and d) after preparing the ITO layer. e) Energy band diagram of the CIGS heterojunction PD. f) I - V curves under illumination of an 808 nm laser at different power densities. g) The wavelength-dependent maximum responsivity and detectivity at zero bias. h) Transient I - t curve of the CIGS heterojunction PD under an 808 nm laser illumination of 127.39 mW cm^{-2} at zero bias. i) An enlarged I - t curve of a period to display the four-stage photoresponse behavior with insets the schematic diagrams of the fundamental working mechanisms of different stages by the pyro-phototronic effect.

well-defined multilayer structure and the length of the nanowires is ≈ 800 nm, implying the excellent rectification behavior and photoresponse of this innovative CIGS heterojunction PD. Figure 1c,d gives the top-view microscopies of the as-synthesized ZnO nanowires with and without the ITO layer, respectively. The nanowires are homogeneously distributed with an averaged diameter of ≈ 90 nm, and it seems that the ITO is covered on the top side of the ZnO nanowire like a mushroom, which is similar to the previous result.^[39] To determine the crystal structure of the heterojunction, the X-ray diffraction was characterized and given in Figure S1 (Supporting Information). There are mainly three kinds of diffraction peaks of the Mo, CIGS, and ZnO, and the appearance of the (0002) peak at $\approx 34.4^\circ$ indicates that the ZnO nanowire is a *c*-axis oriented hexagonal wurtzite structure, enabling the potential of the pyro/piezoelectric effect.^[14,20] The energy band schematic diagram of the CIGS heterojunction is shown in Figure 1e. Different from the usual single-junction structures, there exist two depletion regions at the interfaces of the ZnO/CdS and CdS/CIGS, respectively. The step-like alignment of the PD ensures that the photo-generated carriers in the CIGS layer can be easily separated with the electrons transported into the ITO layer and then collected by the Ag electrode, and holes swept into the bottom Mo electrode, resulting in the output photocurrent. Previously, most researches were mainly concentrated on the optimization of the band structure profile of the CdS/CIGS junction as it was in the photoactive region and could be expected to effectively modulate the separation and transport of the carriers,^[40,41] while the band structure of the ZnO/CdS junction was usually neglected. However, although the interface field in the ZnO/CdS junction is not favorable to the direct separation of the photo-excited carriers, it plays a vital role in determining the transport of the separated carriers and thus can be utilized to tune the photoresponse performances.

The current–voltage (*I*–*V*) characteristics of the CIGS heterojunction PD are measured under illumination of different lasers ranging from 405 to 1550 nm, as illustrated in Figure 1f and Figure S2 (Supporting Information). The dark curve exhibits an outstanding rectification behavior with a rectification ratio of 180.5, which is ensured by forming the good multilayer hetero-

junction. Besides, the output current is strongly dependent on the laser wavelength, but substantial photoresponse behaviors can be found at the zero bias when the laser wavelength is lower than 1550 nm, and the photocurrents of different lasers are all nearly linearly proportional to the power density in the range of 1.27 to 127.39 mW cm⁻² (Figure S3a, Supporting Information). These results indicate that the CIGS heterojunction has a good quality, and achieves an excellent photovoltaic property, demonstrating its significant potential application in self-powered PDs. However, as the 1550 nm is outside the light absorption range of the heterojunction, nearly no photoresponse can be observed under illumination of all the power densities, which is one of the most significant disadvantages of the solar cell structures in developing as broadband PDs.^[14,31] For a PD, one of the key parameters is the *R*, which represents the response sensitivity to an optical input, and another key figure of merit is the specific *D*, which reflects the detecting capacity of a weak signal. Based on the corresponding equations in the Supporting Information, the power density-dependent *R* and *D* results of different lasers are calculated and summarized in Figure S3b–f (Supporting Information). The *R*, as well as the *D*, exhibits a general decreasing tendency with the power density, which is similar to the previous results.^[10,14] The wavelength-dependent maximum *R* and *D* results at the 1.27 mW cm⁻² are derived and given in Figure 1g. As the output current, the *R* and *D* also shows a strong dependence on the laser wavelength and the best *R* of 0.455 A W⁻¹, and *D* of 7.22×10^{11} Jones are obtained for the 808 nm, which can be ascribed to its higher external quantum efficiency as previously reported in this heterostructure.^[18,31] It is obvious that these results are not only better than the best results of the similar heterostructures at zero bias, but also far exceed those observed in other heterojunctions under enormous external voltages, as summarized in **Table 1**.

Figure 1h gives a typical current–time (*I*–*t*) result of the PD at zero bias under an 808 nm laser illumination of 127.39 mW cm⁻². The similar to the previous results of the ZnO nanowire-based devices, a dynamic four-stage current behavior can be obviously observed, demonstrating that the pyroelectric field is formed in the ZnO nanowire and can be utilized to effectively modulate the photoresponses due to

Table 1. Comparison of Photoresponse Performances for Multilayer Heterojunction-Based PDs.

Device structure	Spectral range	Bias voltage [V]	Responsivity [A W ⁻¹]	Detectivity [Jones]	References
Mo/CIGS/CdS/ZnO film/ITO	300–1100 nm	0	0.41	3.08×10^{11}	[15]
ZnO nanowire/MAPbI ₃ /spiro-OMeTAD	≈ 325 nm	0	0.0083	1.3×10^{10}	[19]
Mo/CZTSSe/CdS/ZnO/ITO	300–1100 nm	0	0.39	2.04×10^{11}	[42]
Mo/CZTSSe/CdS/ZnO/ITO	300–900 nm	0	0.22	2.69×10^{11}	[43]
ZnO nanowire/Graphene/CdS	≈ 365 – ≈ 550 nm	0	0.0273	/	[44]
ITO/CuI/FeS ₂ /ZnO	300–1100 nm	0	0.017	/	[45]
ITO/ZnO nanowire/Si	360–1064 nm	1	0.0676	3.1×10^{10}	[38]
ITO/ZnO nanowire/CsPbI ₂ /spiro-OMeTAD	≈ 300 –540 nm	1	0.14	7.0×10^{11}	[46]
AZO/ZnO/PVK/PEDOT:PSS	≈ 300 – ≈ 450 nm	-5	0.0816	3.5×10^9	[47]
ITO/ZnO/PFN/Bphen/4CzIPN/NPB	350–620 nm	-1.5	0.03	2.88×10^{11}	[48]
ZnO nanowire/PbS	300–1000 nm	-10	0.051	3.4×10^8	[49]
Mo/CIGS/CdS/ZnO nanowire/ITO	405–1064 nm	0	0.455	7.22×10^{11}	This work

the pyroelectric effect. To illustrate the transient photoresponse mechanism, an enlarged $I-t$ curve of one period is systematically presented in Figure 1i, and the four-stage dynamic characteristic (marked as I, II, III, and IV, respectively) can be understood as follows:^[19,20,33] first, the current always keeps the initial dark current (I_{dark}) in dark. When a laser is suddenly turned on at stage I, electron-hole pairs induced in the CIGS layer are separated to the top and bottom electrodes to contribute to the output photocurrent (I_{photo}) due to the photovoltaic effect. Meanwhile, a rapid rise of the temperature ($dT/dt > 0$) in the ZnO nanowire is also induced, which could result in a pyroelectric field, then the transport of the electrons is facilitated and an additional pyroelectric current (I_{pyro}) is also generated, the phenomenon of which is called as Pyro-phototronic effect.^[19–21] As the pyroelectric field is in alignment with the built-in field, the I_{pyro} peak is positively accumulated on the I_{photo} , as shown in Figure 1i. Under a sustained illumination at stage II, the I_{photo} keeps still. While the temperature tends to a constant heating state at this stage (meaning there is no temperature variation, $dT/dt = 0$), then the pyroelectric field fades away, thus the pyroelectric current resulting from the pyroelectric effect quickly vanishes. When suddenly turning off the illumination at stage III, the photovoltaic current (I_{photo}) quickly decreases to zero as there are no photo-generated carriers in the heterojunction. However, a rapid temperature decrease ($dT/dt < 0$) could cause an opposite pyroelectric field in the ZnO nanowire. As here the field direction is contrary to that of the built-in field, a reverse pyroelectric current (I_{pyro}) peak lower than the I_{dark} is produced. Finally, when staying in a stable dark condition at stage IV, the whole device returns to room temperature. As a result, the opposite pyroelectric field, along with the induced I_{pyro} , vanishes accordingly, and the output current decreases to the initial I_{dark} again.

To determine the impacts of the pyroelectric effect on the spectral range in the CIGS heterojunction PD, the transient $I-t$ curves are first studied under illumination of these different lasers at 127.39 mW cm⁻² and zero bias, as illustrated in Figure 2a. The same as the $I-V$ results due to the photovoltaic effect, the large stable photovoltaic current can be obtained upon illumination of 405, 532, 671, 808, and 1064 nm lasers at the continuous laser on stage, but it is still nearly zero upon the 1550 nm laser illumination due to the absence of the photo-generated carriers. While, quite different from them, the periodic peaks of the pyroelectric currents are observed in the whole wavelength range at the transient laser on and off stages with good reproducibility, indicating an exceptional spectral broadening property of the pyroelectric effect in the CIGS heterojunction. Besides, the pyroelectric response also highly depends on the laser wavelength but with a more or less difference from the photovoltaic response. Typically, the I_{photo} of the 1064 nm is lower than that of the 532 nm, but it is just reverse for the I_{pyro} or I_{pyro} , which can be attributed to their different working mechanisms. It is generally suggested that a longer wavelength could result in a larger temperature rise,^[25] then the temperature variation, together with the pyroelectric potential, should raise slightly with an increase of the laser wavelength, thus it is thought to achieve a gradually improved pyroelectric response. However, besides the pyroelectric potential, the pyroelectric response also shows a strong dependence on the number of

the separated carriers in the ZnO/CdS interface, which can make full use the advantage of the pyroelectric effect.^[33,38] The number of these carriers increases with the laser wavelength adding from 405 to 808 nm due to the enhanced photovoltaic conversion efficiency,^[18,31] so that the amplitude of the pyroelectric current peak also enhances gradually. When the wavelength increases again, the conversion efficiency starts to decay, resulting in a reduction of the number of the separated carriers, then the pyroelectric response should also decrease accordingly. From the above discussion, it is concluded that the pyroelectric response is dependent on both the pyroelectric field and the photo-generated carriers (photovoltaic effect), that may be why the wavelength dependency is different for the photovoltaic and pyroelectric responses.

To well show the wavelength-dependent improvement of the photoresponses by the pyroelectric effect, the enhancement ratios of $(I-I_{\text{photo}})/I_{\text{photo}}$ are calculated and given in Figure 2c. It is noteworthy that although the photoresponse is very low for the 1550 nm, the highest ratio of 34.010% is obtained mainly due to the near-zero photovoltaic current, confirming the outstanding broadband photoresponse of the pyroelectric effect. Besides, the ratio exhibits a general increasing tendency except for the 405 nm, which is consistent with the wavelength-dependent pyroelectric field. The relatively larger ratio of the 405 nm in the range of 405–1064 nm may result from the photovoltaic absorption loss by the amorphous CdS layer, which could give rise to a lower photovoltaic response. To well illustrate the photoresponse improving and wavelength enlarging behaviors induced by the pyroelectric effect, the band structure diagrams are given in Figure 2d,e. When a pulsed laser of the 405–1064 nm is illuminated on the CIGS heterojunction PD, most of photons are absorbed by the CIGS, and the photo-excited electron-hole pairs are separated by the interface field of the CdS/CIGS junction with the electrons and holes transported upward and downward, respectively, as shown in Figure 2e. The holes can be directly collected by the Mo electrode, while the electrons should first transport from the interface of the ZnO/CdS junction and then contribute to the output current. Therefore, the ZnO/CdS interface plays a vital role in the transport and final collection of the electrons. At the laser on stage, a forward pyroelectric field is induced due to a rapid rise of the temperature in the ZnO nanowire with the negative pyro-charges distributing at the ZnO/CdS interface and the positive pyro-charges located at the ITO/ZnO interface, and it would accelerate the transport of the separated electrons toward from the ZnO/CdS junction to the ITO electrode, thus an instant improvement of the photocurrent is induced. While for the irradiation of the 1550 nm laser, there are no photo-generated electron-hole pairs as it is beyond the absorption range of the CIGS layer, as presented in Figure 2e. However, the pyroelectric potential could still be produced in the ZnO nanowire due to the photothermal effect, and it would modulate the distribution of the coherent carriers in the heterojunction. Therefore, an instantaneous pyroelectric current is also achieved. On the contrary, when the laser is suddenly turned off, a backward pyroelectric field is formed in the ZnO nanowire due to an opposite distribution of the pyro-charges. At this time, the pyroelectric field would drive the electrons away from the ZnO/CdS interface, resulting in a transient reverse pyroelectric current.

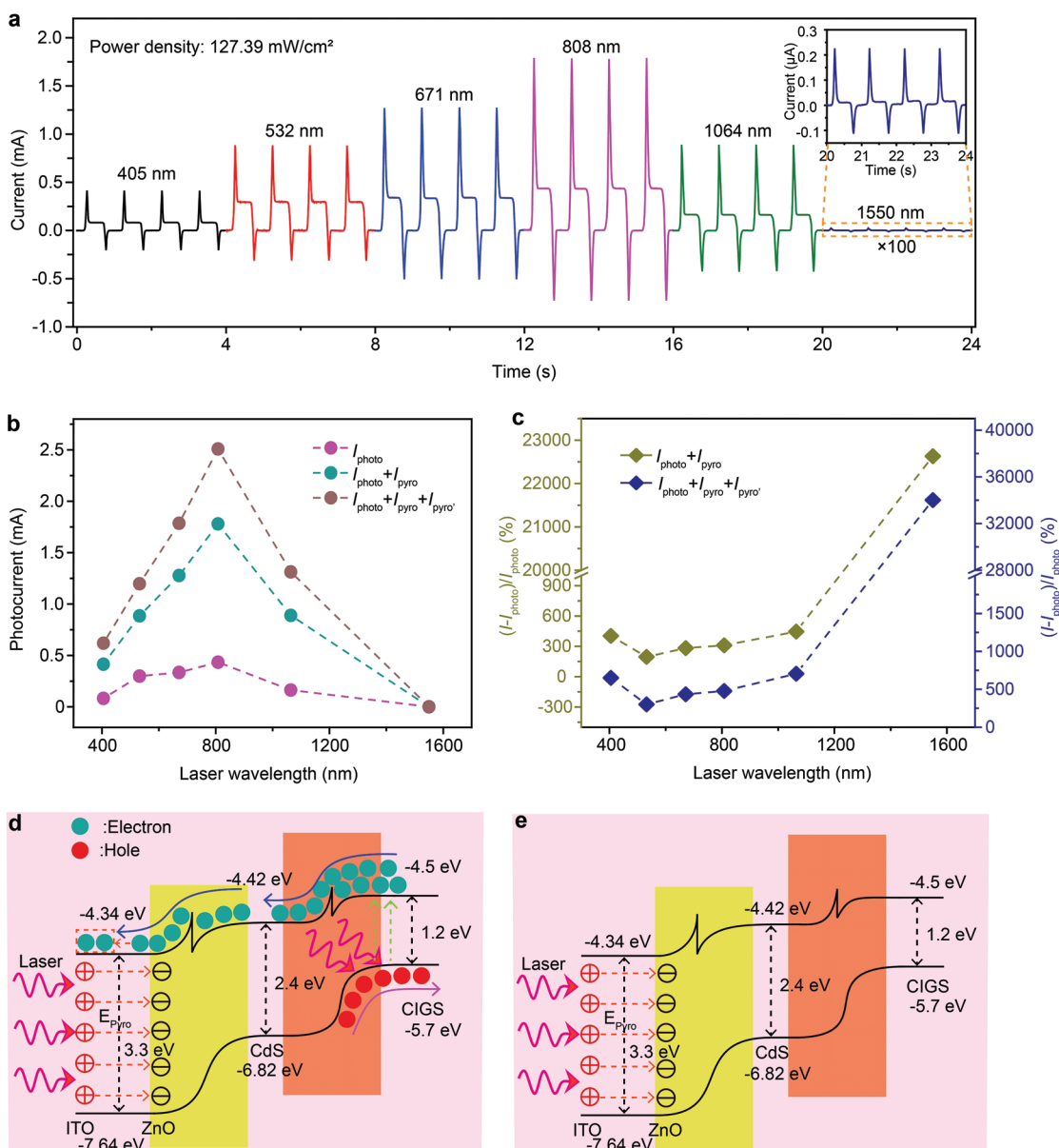


Figure 2. a) Transient $I-t$ curves of the CIGS heterojunction PD under illumination of different wavelength lasers at $127.39 \text{ mW cm}^{-2}$, with inset the enlarged result upon 1550 nm laser illumination. The extracted b) photocurrents and c) photocurrent enhancement ratios as a function of the laser wavelength. Energy band diagram of the CIGS heterojunction PD induced by the pyroelectric effect under illumination d) in and e) out of the light absorption region.

Then, the pyroelectric effect on the power density is well studied. **Figure 3a** gives the systematic $I-t$ results of the CIGS heterojunction PD under illumination of an 808 nm laser at different power densities of 1.27 to $127.39 \text{ mW cm}^{-2}$. The four-stage photocurrent behavior is clearly observed in the whole power density range, demonstrating the excellent coupling of the photovoltaic and pyroelectric effects. Moreover, the photoreponse improves gradually with the power density, and it seems that the photovoltaic current (I_{photo}) and the pyroelectric current (I_{pyro} or $I_{\text{pyro}'}$) are all linearly proportional to the power density, as summarized in **Figure 3b**. However, the enhancement ratio shows a nonmonotonic changing tendency, and the maximum

ratios of 405.5% and 605.5% are obtained at 1.27 mW cm^{-2} for the $I_{\text{pyro}}/I_{\text{photo}}$ and $(I_{\text{pyro}} + I_{\text{pyro}'})/I_{\text{photo}}$, respectively, as shown in **Figure 3c**. The power density-dependent R and D results are then calculated and given in **Figure 3d,e**. The maximum R_{photo} and D_{photo} are still about 0.455 A W^{-1} and $7.22 \times 10^{11} \text{ Jones}$ at 1.27 mW cm^{-2} , respectively, which are consistent with the $I-V$ results, demonstrating the stable self-powered property induced by the photovoltaic effect. When the pyroelectric effect is introduced, the R_{photo} is dramatically improved to $R_{\text{photo}} + R_{\text{pyro}}$ and $R_{\text{photo}} + R_{\text{pyro}} + R_{\text{pyro}'}$ with the maximum responsivities of 2.3 and 3.21 A W^{-1} , which are enhanced by 505.5% and 705.5% , respectively, and the D_{photo} are greatly enhanced to $D_{\text{photo}} + D_{\text{pyro}}$

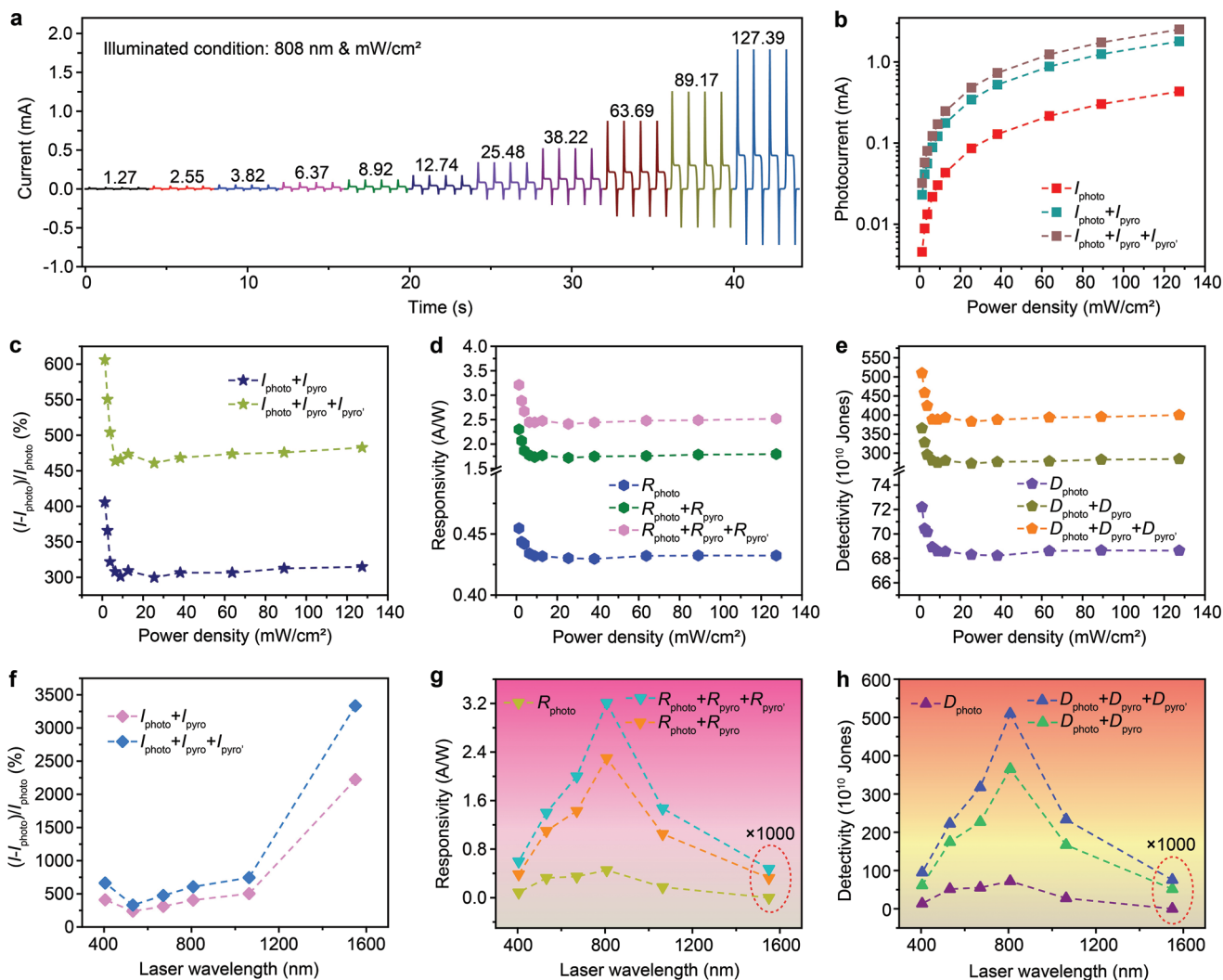


Figure 3. a) Transient I - t curves of the CIGS heterojunction PD under illumination of an 808 nm laser at different power densities. The extracted b) photocurrents, c) photocurrent enhancement ratios, d) responsivities, and e) detectivities as a function of the power density. The laser wavelength-dependent maximum f) photocurrent enhancement ratios, g) responsivities, and h) detectivities.

and $D_{\text{photo}} + D_{\text{pyro}} + D_{\text{pyro}'}$ with the maximum detectivities of 3.75×10^{12} and 5.23×10^{12} Jones, which get increments of 519.4% and 724.4%, respectively, demonstrating the substantial photovoltaic response improvements by the pyroelectric effect in the CIGS heterojunction PD.

Moreover, the transient I - t characteristics of the different power densities are also systematically studied under illumination of the other lasers of 405, 532, 671, 1064, and 1550 nm, respectively, and the similar four-stage photocurrent and photo-response improvement behaviors can be obtained, as shown in Figures S4-S8 (Supporting Information). The wavelength-dependent maximum enhancement ratios of the $I_{\text{pyro}}/I_{\text{photo}}$ and $(I_{\text{pyro}} + I_{\text{pyro}'})/I_{\text{photo}}$ are summarized in Figure 3f. For 405 nm, the maximum photocurrent enhancements are observed at 89.17 mW cm^{-2} with the $I_{\text{pyro}}/I_{\text{photo}}$ ratio of 409.9% and the $(I_{\text{pyro}} + I_{\text{pyro}'})/I_{\text{photo}}$ ratio of 662.8%. While for 532 nm, the maximum ratios are decreased to 238.5% and 330.8%, respectively, which are obtained at 1.27 mW cm^{-2} . With an increase

of the laser wavelength gradually, the maximum ratios start to rise slowly and reach 503.2% and 744.5% for the 1064 nm laser illumination, respectively. When the laser wavelength extends again to 1550 nm, both the $I_{\text{pyro}}/I_{\text{photo}}$ and $(I_{\text{pyro}} + I_{\text{pyro}'})/I_{\text{photo}}$ ratios are greatly enhanced with the best values of 22607% and 34010% observed at 127.39 mW cm^{-2} . Besides, the laser wavelength-dependent maximum R and D results are also extracted and presented in Figure 3g,h. The R_{photo} , as well as the D_{photo} , has the same value and exhibits the same wavelength dependency as the results in Figure 1g, further confirming the stable and reliable self-powered property. More importantly, the significant improvements induced by the pyroelectric effect are obviously achieved in the whole wavelength range. In particular, the best R and D at the 808 nm are far better than the results in any pyroelectric effect-modulated ZnO-based heterojunctions reported till now. Even the maximum R and D at 1550 nm can also be comparable to the best results in these systems, as shown in Table 2, demonstrating the excellent photoresponse

Table 2. Comparison of Photoresponse Performances for ZnO Nanowire-Based PDs Induced by Pyroelectric Effect.

Device structure	Laser wavelength [nm]	Bias voltage [V]	Responsivity [mA W^{-1}]	Detectivity [Jones]	Response time [μs]	References
ZnO nanowire/MAPbI ₃ /spiro-OMeTAD	325 nm	0	26.7	4.0×10^{10}	53/63	[19]
ZnO nanowire/Si	325 nm	0	13	1.4×10^9	19/22	[23]
ZnO nanowire/Si	325 nm	0	17	/	700	[24]
ZnO nanowire/ZnTe	325 nm	0	196.24	3.47×10^{12}	62/109	[25]
FTO/ZnO/Cu ₂ O ₃ /ITO/AgNWs	365 nm	0	488	3.66×10^9	7/10	[26]
ZnO/NiO	365 nm	0	290	2.75×10^{11}	3.92/8.9	[27]
ITO/ZnO/Si/Ag	442 nm	0	79.9	2.5×10^{10}	600/500	[28]
Si/SnO _x /ZnO/ITO	650 nm	0	64.1	2.4×10^{11}	2/1	[29]
ITO/ZnO nanowire/PEDOT:PSS	325 nm	0	3.5	7.5×10^9	$5.8 \times 10^3/7.3 \times 10^3$	[33]
Si/ZnO nanowire/PEDOT:PSS	648 nm	0	22.054	/	/	[37]
Mo/CIGS/CdS/ZnO nanowire/ITO	808 nm	0	3.21×10^3 (1 Hz)	5.23×10^{12} (1 Hz)	67.13/78.57	This work
Mo/CIGS/CdS/ZnO nanowire/ITO	1550 nm	0	0.475 (1 Hz)	7.55×10^8 (1 Hz)	67.13/78.57	This work
Mo/CIGS/CdS/ZnO nanowire/ITO	808 nm	0	4.92×10^3 (500 Hz)	7.81×10^{12} (500 Hz)	67.13/78.57	This work
Mo/CIGS/CdS/ZnO nanowire/ITO	1550 nm	0	0.719 (500 Hz)	1.14×10^9 (500 Hz)	67.13/78.57	This work
Mo/CIGS/CdS/ZnO nanowire/ITO	808 nm	0	7.22×10^3 (pyro + piezo)	1.17×10^{13} (pyro + piezo)	50.17/60.65	This work
Mo/CIGS/CdS/ZnO nanowire/ITO	1550 nm	0	0.855 (pyro + piezo)	1.36×10^9 (pyro + piezo)	50.17/60.65	This work

enhancement and spectral broadening properties of the pyroelectric effect in the CIGS heterojunction.

As the temperature variation is the basis and origin of the pyroelectric field, the working temperature is suggested to play an essential role in the pyroelectric effect. Therefore, some researchers have even modulated the pyroelectric responses by changing the ambient temperatures, which were realized by either placing the device in a different environment or applying an external bias to the device.^[19,20,23,24,33] Besides, this can also be utilized to check the working mechanism of the intrinsic pyroelectric effect. Then, to further illustrate the pyroelectric effect in the CIGS heterojunction, the transient $I-t$ curves are also measured under illumination of an 808 nm laser at 1.27 mW cm^{-2} and different biases ranging from 0 to 0.55 V, as shown in Figure S9 (Supporting Information). The four-stage current behavior can be obviously obtained when the bias voltage is lower than $\approx 0.45 \text{ V}$. With increasing the bias voltage, the I_{dark} increases substantially, but there is nearly no variation for the I_{photo} , which is a typical characteristic in solar cell structures at the forward biases less than the open voltages.^[10,31] In addition, it is observed that the pyroelectric current peak decreases gradually and disappears at last, which is also similar to the previous results,^[19,20,23] and can be understood as follows: a background temperature of the PD, which could result in the reduction of the temperature variation induced by the transient laser illumination, is generated due to the Joule heat effect caused by the dark current, and the background temperature increases gradually with increasing the I_{dark} , then the transient temperature variation, together with the pyroelectric potential, is forced to weaken, thus the pyroelectric response decreases accordingly and disappears at last.

In addition, the temperature variation is also related to the turn on/off time,^[20] then the transient photoresponse of the CIGS heterojunction PD is investigated under an 808 nm

laser illumination of 1.27 mW cm^{-2} with different frequencies ranging from 1 to 500 Hz, and the $I-t$ results are presented in Figure 4a. Obviously, a nearly constant I_{photo} is observed in the frequency range, indicating its excellent capability of following the high-frequency pulsed signals based on the photovoltaic effect, which may be attributed to the excellent transport property of the ZnO nanowire arrays. While, both the I_{pyro} and the $I_{\text{pyro}'}$ get enhanced gradually with an increase of the frequency at first, and then tend to be unchanged when the frequency is larger than 100 Hz, resulting in the first increase and then saturation relations for the $I_{\text{photo}} + I_{\text{pyro}}$ and $I_{\text{photo}} + I_{\text{pyro}} + I_{\text{pyro}'}$, as shown in Figure 4b. As the pulse laser is gotten by a mechanical chopper with different frequencies, the turn on/off time for a laser beam of a constant area should decrease gradually with increasing the frequency. Therefore, the pyroelectric potential, as well as the pyroelectric response, would increase due to the raised temperature variation (dT/dt). However, the transport of the carriers can only be facilitated by the pyroelectric field to some extent due to the limited number of separated carriers in the heterojunction. With the pyroelectric field increasing gradually, the modulation of the transport property tends to be optimized, that may be why the pyroelectric response nearly keeps constant at very high frequencies. Figure 4d,e gives the frequency-dependent R and D results, respectively. The $R_{\text{photo}} + R_{\text{pyro}}$ and $R_{\text{photo}} + R_{\text{pyro}} + R_{\text{pyro}'}$ are further improved to 3.38 and 4.92 A W^{-1} , and the $D_{\text{photo}} + D_{\text{pyro}}$ and $D_{\text{photo}} + D_{\text{pyro}} + D_{\text{pyro}'}$ are enhanced to 5.36×10^{12} and 7.81×10^{12} Jones by tuning the laser frequency from 1 to 500 Hz, respectively, indicating that the pyroelectric effect can be more beneficial to the photoresponse by increasing the frequency in a specific range.

The response speed, which is another key factor of a PD, is also studied in this CIGS heterojunction. The typical amplified $I-t$ curves of one period at 1 and 500 Hz, are illustrated in Figure 4f,g, respectively, where the rise time is determined

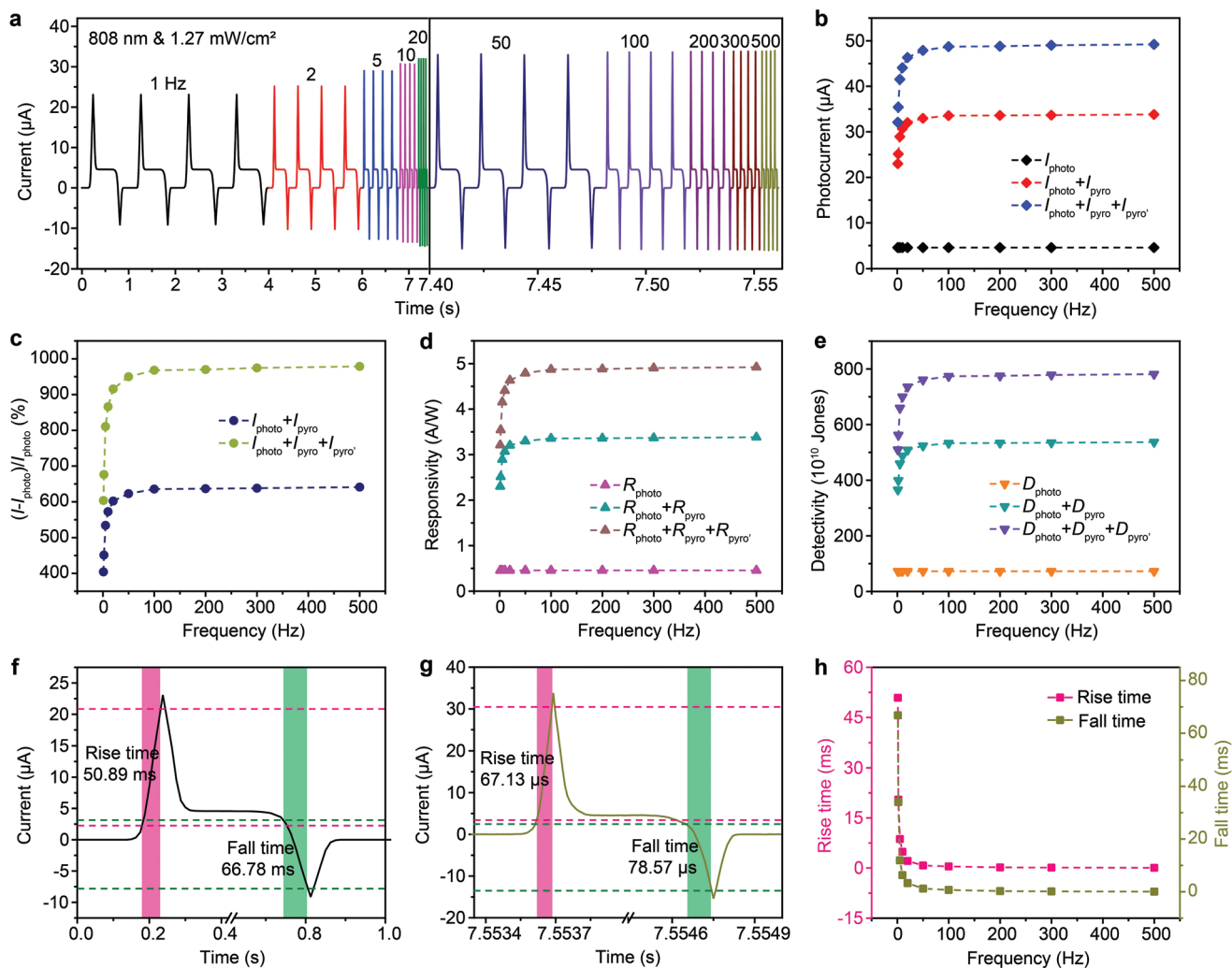


Figure 4. a) Transient $I-t$ curves of the CIGS heterojunction PD under illumination of an 808 nm laser at 1.27 mW cm^{-2} with different frequencies. The extracted b) photocurrents, c) photocurrent enhancement ratios, d) responsivities, and e) detectivities as a function of the frequency. Amplified $I-t$ curve of a period to determine the response times at f) 1 Hz and g) 500 Hz. h) Frequency-dependent rise and fall times.

by the time interval of the output current extending from 10% to 90% at the laser on stage, and the fall time is evaluated by the time interval of the output current decaying from 90% to 10% at the laser off stage. The response time is obtained to be 50.89/66.78 ms under illumination of a 1 Hz laser, and it quickly decreases with increasing the laser frequency, as given in Figure 4h. When the laser frequency reaches 500 Hz, the response time drops to a minimum of 67.13/78.57 μs . The significant improvement in the response speed also demonstrates that the temperature variation-induced pyroelectric field in the ZnO nanowire can indeed vastly promote the transport behavior of the separated carriers in the CIGS heterojunction.

Considering the similar charge polarization effect, the piezoelectric potential can also be induced in the ZnO nanowire when applying an external pressure on the CIGS heterojunction PD, then the piezoelectric effect is utilized to further modulate the photoresponses. The transient $I-t$ curves under illumination of an 808 nm laser at 1.27 mW cm^{-2} and 500 Hz and different vertical pressures of 0 to 2.0 MPa are systematically

measured and presented in Figure 5a. Both the stable I_{photo} and the transient $I_{\text{pyro}}/I_{\text{pyro}'}$ get enhanced with increasing the external pressure, demonstrating the simultaneous improvement of the photovoltaic and pyroelectric effects by the piezoelectric effect. Under compressive strain, the piezoelectric polarization charges could be yielded in the ZnO nanowire with negative charges distributed at the top side and positive charges located at the bottom side close to the interface of the ZnO/CdS.^[50,51] However, it is slightly different from the transient pyroelectric effect, here the negative and positive piezoelectric charges could preferentially repel the holes in the ZnO and attract the electrons in the CdS away from and moving toward their interface, respectively, then the triangular barrier at the ZnO/CdS junction gets downward. Therefore, the separated electrons from the CdS/CIGS junction can easily pass through the barrier and enter the ZnO layer to be transported and collected by the electrode. Meanwhile, the pyroelectric field can also more efficiently facilitate the transport of the separated carriers from the interface of the ZnO/CdS. Therefore, both the

photovoltaic and pyroelectric responses are considerably promoted. Figure 5b gives the pressure-dependent photocurrent results. With the pressure adding from 0 to 2.0 MPa, the $I_{\text{photo}} + I_{\text{piezo}}$ increases from 4.55 to 5.51 μA , the $I_{\text{photo}} + I_{\text{piezo}} + I_{\text{pyro}}$ increases from 33.81 to 47.62 μA , and the $I_{\text{photo}} + I_{\text{piezo}} + I_{\text{pyro}} + I_{\text{pyro}'}$ increases from 49.22 to 72.18 μA . As a result, the enhancement ratios are further improved, and the maximum ratios of $I_{\text{piezo}}/I_{\text{photo}}$, $(I_{\text{piezo}} + I_{\text{pyro}})/I_{\text{photo}}$, and $(I_{\text{piezo}} + I_{\text{pyro}} + I_{\text{pyro}'})/I_{\text{photo}}$ are observed to be 21.1%, 946.6%, and 1486.8%, respectively, as shown in Figure 5c. Besides, the R and D parameters under each pressure are also deduced and summarized in Figure 5d,e, respectively. The maximums of 0.55, 4.76, and 722 A W^{-1} are observed for the $R_{\text{photo}} + R_{\text{piezo}}$, $R_{\text{photo}} + R_{\text{piezo}} + R_{\text{pyro}}$, and $R_{\text{photo}} + R_{\text{piezo}} + R_{\text{pyro}} + R_{\text{pyro}'}$, which are enhanced by 121.1%, 1046.6%, and 1586.8%, respectively, and the best results of 8.97×10^{11} , 7.75×10^{12} , 1.17×10^{13} Jones are obtained for the $D_{\text{photo}} + D_{\text{piezo}}$, $D_{\text{photo}} + D_{\text{piezo}} + D_{\text{pyro}}$, and $D_{\text{photo}} + D_{\text{piezo}} + D_{\text{pyro}} + D_{\text{pyro}'}$, which get improvements of 124.2%, 1073.3%, and 1620.5%, respectively.

Furthermore, the pressure-dependent transient photoreponses of the CIGS heterojunction PD are also studied under illumination of the other lasers, with the $I-t$ curves shown in Figures S10-S14 (Supporting Information). Upon illumination of the 405, 532, 671, and 1064 nm lasers, the photocurrent, enhancement ratio, responsivity and detectivity are all increased monotonously with the pressure similar to the results of the 808 nm but with some different enhancements. Not only that, it is observed that the pyroelectric response improvement is also induced by externally applied pressures for the 1550 nm not located in the photovoltaic response region as the pyroelectric field can easily drive away and attract the coherent carriers in the interface of the ZnO/CdS due to the optimized band alignment of the heterojunction, further confirming the effective optimizations of the carriers' extraction and transport for both the photovoltaic and pyroelectric effects through applying external pressures. The maximum R and D results of each laser wavelength are extracted and given in Figure 5f,g, respectively. The same wavelength dependency can still be observed after

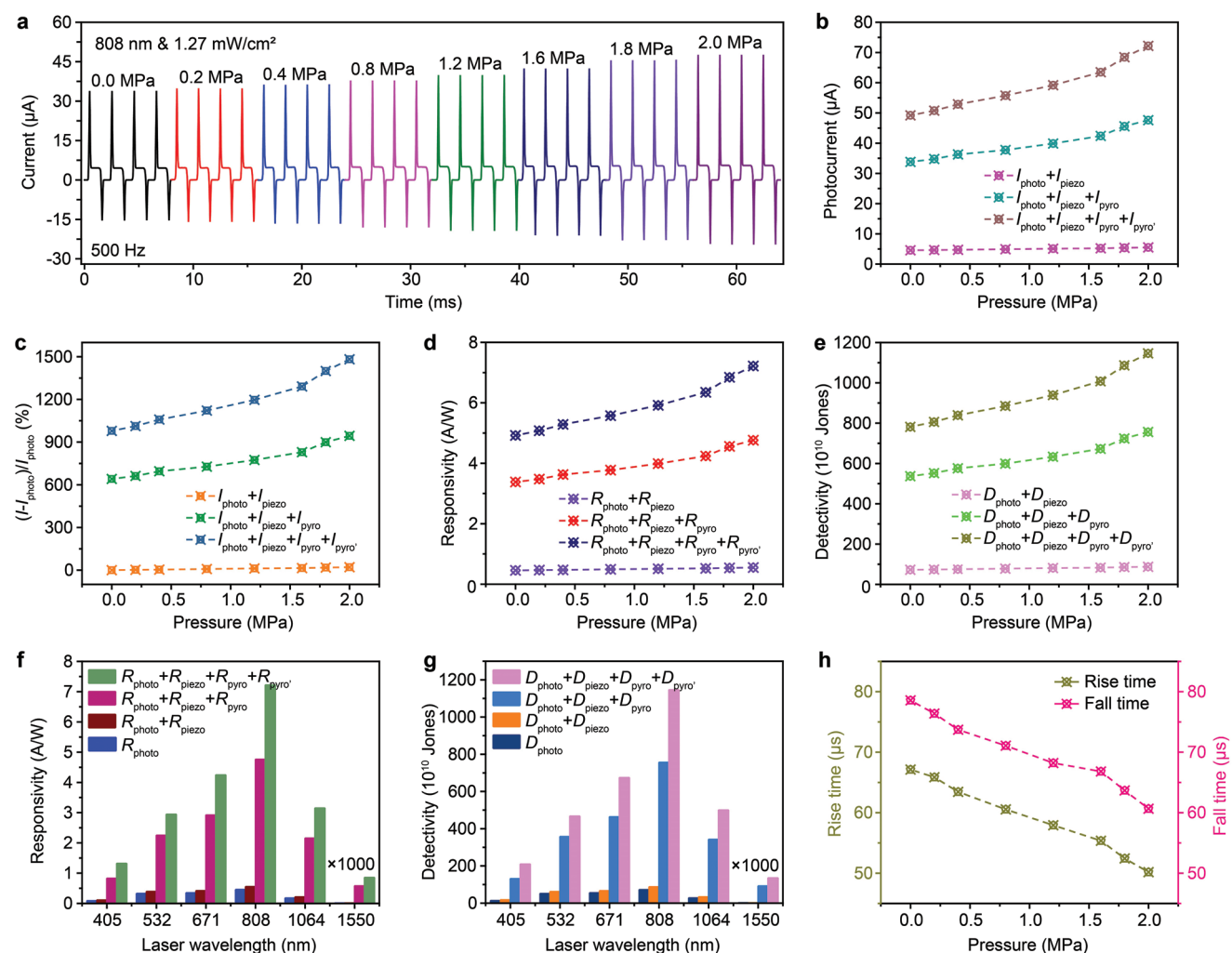


Figure 5. a) Transient $I-t$ curves of the CIGS heterojunction PD under illumination of an 808 nm laser at 1.27 mW cm^{-2} and 500 Hz with different external pressures. The extracted b) photocurrents, c) photocurrent enhancement ratios, d) responsivities, and e) detectivities as a function of the pressure. The laser wavelength-dependent maximum f) responsivities and g) detectivities under an external pressure of 2 MPa. h) External pressure-dependent rise and fall times.

introducing the piezoelectric effect, suggesting that the tuning of the photoresponse has a nearly linear relationship with the external pressure for all laser wavelengths. Besides, after introducing the piezoelectric effect, the response time also descends gradually with the pressure due to the optimized band alignment of the CIGS heterojunction, as shown in Figure 5h. The best rise and fall times of 50.17 and 60.65 μs are obtained at the pressure of 2.0 MPa, which are reduced by 25.3% and 22.8%, respectively.

At last, the transient $I-t$ curves of the ZnO film-based CIGS heterojunction of Glass/Mo/CIGS/CdS/ZnO film/ITO were measured under illumination of an 808 nm laser at different power densities, as shown in Figure S15 (Supporting Information). The photovoltaic response can be clearly observed, and it improves gradually with increasing the power density. However, there is nearly not any pyroelectric peak in the whole power density range, which can be attributed to the amorphous or weak polycrystalline structure of the ZnO film.^[50] Moreover, the transient photocurrent also keeps still without any change for the photovoltaic and pyroelectric responses when external pressures are applied on the device, as shown in Figure S16 (Supporting Information). These results demonstrate that the piezoelectric and pyroelectric effects are indeed originated from the window layer of the ZnO nanowire arrays, and can be well coupled to modulate the photovoltaic responses of the CIGS heterojunction PD, and then achieve high photoresponse, broadband, and fast speed performances.

4. Conclusion

In conclusion, a Cu(In,Ga)Se₂ (CIGS) multilayer heterojunction is successfully prepared and the photoresponses are systematically studied. The heterojunction works well as a self-powered photodetector (PD) with excellent performances of broadband response range of 405 to 1064 nm, large responsivity (R) of 0.455 A W⁻¹, and high detectivity (D) of 7.22×10^{11} Jones, respectively, due to the excellent photovoltaic effect. The pyroelectric effect within the non-photoactive ZnO layer is first utilized to tune the photoresponses of the CIGS heterojunction PD. It is indicated that the temperature variation-induced pyroelectric potential in the ZnO nanowire can effectively accelerate the transport of the separated carriers in the interface of the ZnO/CdS, then the R is increased to 4.92 A W⁻¹ with an increment of 1081.3%, the D is improved to 7.81×10^{12} Jones with an augment of 1081.7%, and simultaneously an ultrafast response time of 67.13/78.57 μs is obtained. Moreover, the response wavelength is enlarged to 1550 nm, which is far beyond the spectral limitation of the CIGS heterojunction. Besides, the piezoelectric effect is further introduced to tune the photovoltaic and pyroelectric responses by optimizing the band alignment of the ZnO/CdS junction when applying the external pressures. Owing to the favorable three-synergistic mechanisms of the photovoltaic, pyroelectric and piezoelectric effects, the best R and D are obtained to be 7.22 A W⁻¹ and 1.17×10^{13} Jones, respectively, and the response time is also shortened to 50.17/60.65 μs , the properties of which are unprecedentedly better than the previous results in the similar structures or other pyro/piezoelectric material-based systems. This work offers deeper understanding

of the pyroelectric and piezoelectric effects on the improvement of the photovoltaic responses in the CIGS multilayer heterojunction PD, and also gives an insight into tuning the performances of the other multilayer heterostructures by introducing the pyro/piezoelectric effects.

Supporting Information

Supporting Information is available from the Wiley Online Library or from the author.

Acknowledgements

This work is supported by the National Nature Science Foundation of China (Grant Nos. 62175058 and U20A20166), the Nature Science Foundation of Hebei Province (Grant Nos. A2022201014), the Science and Technology Plan Project of Hebei Province (Grant No. 216Z1703G), and the Key Research and Development Program of Hebei Province (No. 20314305D).

Conflict of Interest

The authors declare no conflict of interest.

Data Availability Statement

The data that support the findings of this study are available from the corresponding author upon reasonable request.

Keywords

photodetectors, piezo-phototronic effects, pyro-phototronic effect, self-powered, ZnO nanowires

Received: July 27, 2022
Revised: August 29, 2022
Published online: September 25, 2022

- [1] C. F. Pan, L. Dong, G. Zhu, S. M. Niu, R. M. Yu, Q. Yang, Y. Liu, Z. L. Wang, *Nat. Photonics* **2013**, *7*, 752.
- [2] B. S. Ouyang, H. Q. Zhao, Z. L. Wang, Y. Yang, *Nano Energy* **2020**, *68*, 104312.
- [3] S. Cai, X. J. Xu, W. Yang, J. X. Chen, X. S. Fang, *Adv. Mater.* **2019**, *31*, 1808138.
- [4] J. Li, Z. Q. Yuan, C. F. Wang, Z. H. Huo, Q. C. Lu, M. L. Xiong, X. L. Ma, W. C. Gao, C. F. Pan, *Small Sci.* **2022**, *2*, 2100083.
- [5] R. D. Cong, S. Qiao, J. H. Liu, J. S. Mi, W. Yu, B. L. Liang, G. S. Fu, C. F. Pan, S. F. Wang, *Adv. Sci.* **2018**, *5*, 1700502.
- [6] B. J. Shastri, A. N. Tait, T. F. Lima, W. H. P. Pernice, H. Bhaskaran, C. D. Wright, P. R. Prucnal, *Nat. Photonics* **2021**, *15*, 102.
- [7] W. D. Song, J. X. Chen, Z. L. Li, X. S. Fang, *Adv. Mater.* **2021**, *33*, 2101059.
- [8] X. Hu, X. Y. Li, G. Y. Li, T. Li, F. J. Ai, J. H. Wu, W. N. Ha, J. Q. Hu, *Adv. Funct. Mater.* **2021**, *31*, 2011284.
- [9] W. Jiang, T. Zheng, B. M. Wu, H. X. Jiao, X. D. Wang, Y. Chen, X. Y. Zhang, M. Peng, H. L. Wang, T. Lin, H. Shen, J. Ge, W. D. Hu, X. F. Xu, X. J. Meng, J. H. Chu, J. L. Wang, *Light: Sci. Appl.* **2020**, *9*, 160.

- [10] Y. Liu, S. Qiao, H. Sun, J. Liu, L. Guo, Z. Yang, G. Fu, S. Wang, *ACS Appl. Nano Mater.* **2021**, *4*, 1682.
- [11] L. Peng, L. F. Hu, X. S. Fang, *Adv. Funct. Mater.* **2014**, *24*, 2591.
- [12] Z. Wen, J. J. Fu, L. Han, Y. N. Liu, M. F. Peng, L. Zheng, Y. Y. Zhu, X. H. Sun, Y. L. Zi, *J. Mater. Chem. C* **2018**, *6*, 11893.
- [13] L. T. Dou, Y. Yang, J. B. You, Z. R. Hong, W. H. Chang, G. Li, Y. Yang, *Nat. Commun.* **2014**, *5*, 5404.
- [14] S. Qiao, J. H. Liu, X. N. Niu, B. L. Liang, G. S. Fu, Z. Q. Li, S. F. Wang, K. L. Ren, C. F. Pan, *Adv. Funct. Mater.* **2018**, *28*, 1707311.
- [15] Y. Yuan, L. Q. Zhang, G. H. Yan, G. B. Cen, Y. J. Liu, L. L. Zeng, C. X. Zhao, R. J. Hong, W. J. Mai, *ACS Appl. Mater. Interfaces* **2019**, *11*, 20157.
- [16] S. Qiao, Y. Liu, J. Liu, G. Fu, S. Wang, *ACS Appl. Mater. Interfaces* **2021**, *13*, 34625.
- [17] J. C. Yu, X. Chen, Y. Wang, H. Zhou, M. N. Xue, Y. Xu, Z. S. Li, C. Ye, J. Zhang, P. A. Aken, P. D. Lund, H. Wang, *J. Mater. Chem. C* **2016**, *4*, 7302.
- [18] S. Qiao, K. Y. Feng, Z. Q. Li, G. S. Fu, S. F. Wang, *J. Mater. Chem. C* **2017**, *5*, 4915.
- [19] Z. N. Wang, R. M. Yu, C. F. Pan, Z. L. Li, J. Yang, F. Yi, Z. L. Wang, *Nat. Commun.* **2015**, *6*, 8401.
- [20] Y. J. Dai, X. F. Wang, W. B. Peng, C. Xu, C. S. Wu, K. Dong, R. Y. Liu, Z. L. Wang, *Adv. Mater.* **2018**, *30*, 1705893.
- [21] N. Ma, K. W. Zhang, Y. Yang, *Adv. Mater.* **2017**, *29*, 1703694.
- [22] K. W. Zhang, Z. L. Wang, Y. Yang, *ACS Nano* **2016**, *10*, 10331.
- [23] Z. N. Wang, R. M. Yu, X. F. Wang, W. Z. Wu, Z. L. Wang, *Adv. Mater.* **2016**, *28*, 6880.
- [24] J. Q. Dong, Z. J. Wang, X. F. Wang, Z. L. Wang, *Nano Today* **2019**, *29*, 100798.
- [25] D. T. You, C. X. Xu, W. Zhang, J. Zhao, F. F. Qin, Z. L. Shi, *Nano Energy* **2019**, *62*, 310.
- [26] S. Abbas, M. Kumar, D. W. Kim, J. Kim, *Small* **2019**, *15*, 1804346.
- [27] A. K. Rana, M. Kumar, D. K. Ban, C. P. Wong, J. Yi, J. Kim, *Adv. Electron. Mater.* **2019**, *5*, 1900438.
- [28] Y. L. Zhang, M. N. Hu, Z. N. Wang, *Nano Energy* **2020**, *71*, 104630.
- [29] J. P. B. Silva, E. M. F. Vieira, K. Gwozdz, A. Kaim, L. M. Goncalves, J. L. MacManus-Driscoll, R. L. Z. Hoye, M. Pereira, *Nano Energy* **2021**, *89*, 106347.
- [30] Y. J. Zhang, H. X. Su, H. Li, Z. S. Xie, Y. Z. Zhang, Y. Zhou, L. Y. Yang, H. W. Lu, G. L. Yuan, H. W. Zheng, *Nano Energy* **2021**, *85*, 105968.
- [31] J. H. Liu, Z. C. Zhang, S. Qiao, G. S. Fu, S. F. Wang, C. F. Pan, *Sci. Bull.* **2020**, *65*, 477.
- [32] K. Matsubara, P. Fons, K. Iwata, A. Yamada, K. Sakurai, H. Tampono, S. Niki, *Thin Solid Films* **2003**, *431*, 369.
- [33] W. B. Peng, X. F. Wang, R. M. Yu, Y. J. Dai, H. Y. Zou, A. C. Wang, Y. N. He, Z. L. Wang, *Adv. Mater.* **2017**, *29*, 1606698.
- [34] H. Ji, K. W. Zhang, Z. L. Wang, Y. Yang, *Energy Environ. Sci.* **2019**, *12*, 1231.
- [35] Q. Li, J. Huang, J. P. Meng, Z. Li, *Adv. Opt. Mater.* **2022**, *10*, 2102468.
- [36] M. C. Jeong, B. Y. Oh, M. H. Ham, J. M. Myoung, *Appl. Phys. Lett.* **2006**, *88*, 202105.
- [37] W. B. Peng, Z. J. Pan, F. P. Li, Y. H. Cai, Y. N. He, *Nano Energy* **2020**, *78*, 105268.
- [38] S. Qiao, H. J. Sun, J. H. Liu, G. S. Fu, S. F. Wang, *Nano Energy* **2022**, *95*, 107004.
- [39] H. Y. Zou, X. G. Li, W. B. Peng, W. Z. Wu, R. M. Yu, C. S. Wu, W. B. Ding, F. Hu, R. Y. Liu, Y. L. Zi, Z. L. Wang, *Adv. Mater.* **2017**, *29*, 1701412.
- [40] L. Weinhardt, O. Fuchs, D. Grob, G. Storch, E. Umbach, N. G. Dhre, A. A. Kadam, S. S. Kulkarni, C. Heske, *Appl. Phys. Lett.* **2005**, *86*, 062109.
- [41] Y. X. Zhang, Z. J. Hu, S. P. Lin, C. J. Wang, S. Q. Cheng, Z. C. He, Z. Q. Zhou, Y. Sun, W. Liu, *Sol. RRL* **2020**, *4*, 2000290.
- [42] G. H. Yan, C. H. Zeng, Y. Yuan, G. Wang, G. B. Cen, L. L. Zeng, L. Q. Zhang, Y. Fu, C. X. Zhao, R. J. Hong, W. J. Mai, *ACS Appl. Mater. Interfaces* **2019**, *11*, 32097.
- [43] H. Z. Wu, C. H. Ma, J. Y. Zhang, H. C. Cao, R. B. Lin, W. Bai, Z. Q. Pan, J. Yang, Y. Y. Zhang, Y. Chen, X. D. Tang, X. D. Wang, J. L. Wang, J. H. Chu, *ACS Appl. Electron. Mater.* **2021**, *3*, 4135.
- [44] G. Z. Huang, P. P. Zhang, Z. M. Bai, *J. Alloys Compd.* **2019**, *776*, 346.
- [45] Z. Yang, M. Q. Wang, S. Shukla, Y. Zhu, J. P. Deng, H. Ge, X. Z. Wang, Q. H. Xiong, *Sci. Rep.* **2015**, *5*, 11377.
- [46] H. X. Wang, P. F. Zhang, Z. G. Zang, *Appl. Phys. Lett.* **2020**, *116*, 162103.
- [47] X. L. Zhang, J. Li, W. J. Yang, B. Leng, P. J. Niu, X. Jiang, B. D. Liu, *ACS Appl. Mater. Interfaces* **2019**, *11*, 24459.
- [48] D. Zhao, M. G. Wu, R. H. Qin, J. S. Yu, *Opt. Lett.* **2018**, *43*, 3212.
- [49] Z. Zheng, L. Gan, J. B. Zhang, F. W. Zhuge, T. Y. Zhai, *Adv. Sci.* **2017**, *4*, 1600316.
- [50] S. Qiao, J. H. Liu, G. S. Fu, K. L. Ren, Z. Q. Li, S. F. Wang, C. F. Pan, *Nano Energy* **2018**, *49*, 508.
- [51] R. R. Bao, J. Tao, C. F. Pan, Z. L. Wang, *Small Sci.* **2021**, *1*, 2000060.